eprints@whiterose.ac.uk
https://eprints.whiterose.ac.uk/

Impact of Co^{2+} on the spectral, optoelectrical, and dielectric properties of $Mg_{0.25}Ni_{0.25}Cu_{0.5-x}Co_xFe_{1.97}La_{0.03}O_4$ ferrites prepared *via* sol-gel auto combustion route

Ghulam Abbas[a], Atta Ur Rehman[b], Waheed Gull[a], M. Afzaal[a], Nasir Amin[b], Lamia Ben Farhat[c,d], Mongi Amami[c,d], Nicola A. Morley[e], Maria Akhtar[b], Muhammad Imran Arshad[*b], Abdul Ghuffar[a], Abid Mahmood[f], Muhammad Ibrahim[f]

[a] Department of Physics, Riphah International University, Faisalabad Campus, Pakistan.
[b]Department of Chemistry College of Sciences, King khalid university, P.O. Box 9004, Abha, Saudi Arabia
[c]Laboratoire des Matériaux et de l'environnement pour le développement durable LR18ES10. 9 Avenue Dr. Zoheir SAFI, 1006, Tunis, Tunisia
[d]Department of Physics, Government College University, Faisalabad, 38000, Pakistan.
[e]Department of Materials Science and Engineering, The University of Sheffield, UK, S1 3JD
[f]Department of Environmental Sciences & Engineering, Government College University, Faisalabad 38000, Pakistan.

Corresponding author email: miarshadgcuf@gmail.com

Abstract

Spinel ferrites are attaining huge importance in the modern era, due to their incredible properties, which means they are widely used in various fields. Therefore, in this paper a cost-effective and environmentally friendly preparation of $Mg_{0.25}Ni_{0.25}Cu_{0.5-x}Co_xFe_{1.97}La_{0.03}O_4$ (x = 0.0, 0.125, 0.25, 0.375, and 0.5) ferrites *via* the sol-gel auto-combustion method were carried out. How the structural and functional properties varied with the Cu to Co ratio was studied. It was found that the crystallite size (D) was reduced from 47.2 to 27.6 nm as the Co^{2+} increased from x = 0.0 to 0.5. While the two major absorption bands including the higher frequency band (v_1) and lower frequency band (v_2) lie in the range of 573.80 – 538.65 cm^{-1} and 470.37 – 405.65 cm^{-1} belong to the spinel matrix. Five active Raman modes were found in the range of wave number 200 – 800 cm^{-1} corresponds to the sublattices of the spinel structure. The optical bandgap increased from 0.85 eV to 1.33 eV for x = 0.0 to x = 0.25 and then observed optical band gap was 1.15 eV and 1.46 eV for x = 0.375 to x = 0.5. The resistivity (ρ) was minimum for Co^{2+} concentration x = 0.25 at low temperature, while at high temperature the resistivity (ρ) was maximum for Co^{2+} doping x = 0.25. The temperature coefficient of resistance percentage (TCR %) was −2.66%/K at 513 K for x = 0.25, as shown in the graphical abstract. At lower frequencies, the impedance was observed maximum for Co^{2+} doping x = 0.125 and

minimum for $x = 0.375$. These findings indicate that the as-prepared ferrites are a potential candidate for optoelectrical and bolometric devices.

Keywords:
spinel; sol-gel auto-combustion; absorption band; resistivity; temperature coefficient.

1 Introduction

Spinel ferrites are a ceramic material formed by the combination of iron oxide mixed with a quantity of divalent (Ni^{2+}, Zn^{2+}, Cu^{2+}, Cd^{2+}, Mn^{2+}, $Mg^{2+,}$ etc.) and trivalent (La^{3+}, Ce^{3+}, Nd^{3+}, Sm^{3+}, Dy^{3+}, Eu^{3+}, Er^{3+}, and Ho^{3+}) cations. Spinel ferrites have the formula AB_2O_4, where "A" and "B" represent the divalent and trivalent cations, respectively [1]. Ferrites have two types: soft and hard ferrites, with spinel ferrites belonging to the soft ferrites having low coercivity. They can easily be magnetized and demagnetized, also they have high resistivity at room temperature (RT). Soft ferrites are used in biomedical applications [2], cores of transformers [3], drug delivery [4], antennas [5], pharmaceutical [6], sensors [7], high-frequency power [8], and storage devices [9]. From various literature, there are several methods of preparation including the co-precipitation method [10-14], sol-gel auto combustion method [15-17], solid-state method [18], hydrothermal route of preparation [8], which have successfully been used to study the properties of ferrites.

Jnaneshwara *et al.* [19] reported $Co_{1-x}Cu_xFe_2O_4$ nano ferrites synthesized *via* solution combustion route and suggest that the Cu^{2+} doped cobalt ferrites could be used for microwaves devices. It was observed that the crystallite size was increased from 13.37 to 34.54 nm with the addition of Cu^{2+} cations. The absorption bands exist around 382 cm^{-1} and 578 cm^{-1} corresponds to octahedral (*B*-) and tetrahedral (*A*-) sites, respectively. Samavati *et al.* [20] synthesized $Co_{1-x}Cu_xFe_2O_4$ using a cost-effective and easy co-precipitation approach. Also, the authors reported that the increase in Cu^{2+} concentration enhances local disorder at both *A*- sites and *B*-sites in the lattice, according to Raman scattering studies. Pourzaki *et al.* [21] studied Co^{2+} substituted Mg ferrites prepared by standard ceramic method and observed that the crystallite size and lattice constant were increased with the increase of Co^{2+} doping, while Ahmad *et al.* [22] reported $Cu_{1-x}Co_xFe_2O_4$ synthesized by employing the so-gel route and confirmed the formation of spinel matrix Cu-Co ferrites. Pubby *et al.* [23] synthesized Co^{2+} substituted Ni ferrites by sol-gel method. The lattice constant increased with doping of cobalt, while porosity and crystallite size decreased. It was also noted that as the cobalt doping increased, the active modes of Raman spectra shifted to a lower wavenumber. Bharathi *et al.*, [24] reported $CoFe_{1.925}La_{0.075}O_4$ inverse spinel ferrite with secondary phase $LaFeO_3$ and observed that the lattice constant had a value of 8.401 Å. Two separate regions can be seen in temperature-

dependent resistivity curves, indicating two different types of conduction mechanisms. According to the literature study and the best of our knowledge there is no literature present that proposed the synthesis of $Mg_{0.25}Ni_{0.25}Cu_{0.5-x}Co_xFe_{1.97}La_{0.03}O_4$ (Co-MNCLF) spinel ferrites. In this research work Co-MNCLF spinel ferrites with x varies from 0.0 to 0.5 with step interval of 0.125 were prepared by using sol-gel auto-combustion method and reported their structural study, absorption bands, vibrational modes, optical band gap, resistivity and temperature coefficient of resistance.

2 Experimental details

2.1. Material used and preparation method of Co-MNCLF ferrites

$Mg_{0.25}Ni_{0.25}Cu_{0.5-x}Co_xFe_{1.97}La_{0.03}O_4$ (x = 0.0, 0.125, 0.25, 0.375, and 0.5) ferrites were synthesized using the sol-gel auto-combustion method. Following chemicals Mg $(NO_3)_2 . 6H_2O$, Ni $(NO_3)_2 . 6H_2O$, Cu $(NO_3)_2 . 3H_2O$, Co $(NO_3)_2 . 6H_2O$, La $(NO_3)_3 . 6H_2O$, Fe $(NO_3)_3 . 9H_2O$ were used and a stoichiometric amount of these materials were taken and dissolved in distilled water. Citric acid and metal nitrates were added with 1:1. Here, citric acids act as a chelating agent for metal ions and organic fuel during the combustion process. Ammonia was added drop by drop to maintain the as-prepared solution pH to 7. The temperature of the magnetic stirrer was maintained at 80 °C unless the gel was formed and then turned to 300 °C that caused the ash formation. Sintering was performed at 800 °C for 8 h. The obtained Co-MNCLF material was grounded and used for different characterizations. The preparation process steps are depicted in Fig. 1.

2.2. Characterization techniques

To obtain the Bragg angle (2θ) range 20°‒60°, X-ray diffractometer (XRD), D8 Advanced, Bruker, Cu-K$_\alpha$ radiation, and λ = 1.5418 Å was used. Perkin Elmer Infrared (PEIR) Spectrometer was used to record Fourier-transform infrared (FTIR) spectra. This study explained the cation distribution at tetrahedral and octahedral sites in ferrites. Raman spectra were used for the structural and vibrational mode analysis of materials. Perkin Elmer, UV–visible Double Beam (UV-DS) Spectrophotometer Model Lambda 25 used to record the UV-visible spectra. The temperature-dependent electrical properties were determined by two probes current-voltage (I-V) measurement, for this purpose KEITHLEY electrometer model 2401 was used. The dielectric analysis was performed with an IM3536 LCR meter.

3 Results and their discussion of Co-MNCLF ferrites

3.1 X-ray diffraction (XRD) study

The XRD patterns of the Co-MNCLF ferrites at room temperature are shown in Fig. 2. The diffraction peaks (220), (311), (222), (400), (422), and (511), (440) of the Co-MNCLF

compound are well indexed from the origin *via* the higher 2θ values to the crystal planes (JCPDS card no: 34-0425). This corresponds to the *F d -3 m* space group, including secondary phase formation corresponding to orthorhombic structure *LaFeO$_3$* (JCPDS card no: 75-0541). Several researchers have previously observed orthorhombic phases of rare earth substituted ferrites [10, 15]. The high reactivity of Fe^{3+} ions with La^{3+} ions at grain boundaries may have caused the emergence of this second secondary phase [15]. The presence of paramagnetic La^{3+} ion ($0\mu_B$) formed *LaFeO$_3$* was reduced the magnetism and magnetic behaviour [25]. The crystallite size (*D*) of the as-prepared ferrites was calculated by Scherer's formula [11];

$$D = \frac{n\lambda}{\beta Cos\theta} \qquad (1)$$

where n = 0.94, "*β*" indicates the FWHM (full width at half maxima), and "*θ*" is Bragg's angle. The FWHM measured with (311) peaks increased with the addition of Co^{2+} doping, indicating that the crystallite size (*D*) is reduced as the Co^{2+} cations concentration increases. The "*D*" values were reduced from 47.2 to 27.6 nm as the Co^{2+} doping increased from $x = 0.0$ to $x = 0.5$ (Table 1). The graphical representation of FWHM and crystallite size (*D*) are given in Fig. 3 and the reduction in the crystallite size (*D*) may be due to the bond energy of Co–O being greater than Cu–O. Bragg's law was used to determine d-spacing (inter planer spaces) [11];

$$d = \frac{n\lambda}{2sin\theta} \qquad (2)$$

where "*n*" shows the order of diffraction. The lattice constant (*a*) was calculated by the following equation [11];

$$a = d\sqrt{h^2 + k^2 + l^2} \qquad (3)$$

where (*h k l*) are miller indices. The d-spacing (*d*) and lattice constant (*a*) for the ferrites are given in Table 1. As the doping (*x*) increases from $x = 0.0$ to $x = 0.5$, the "*d*" and "*a*" both decrease and graphically are represented in Fig. 4. Vegard's law explains the decreasing trend in the value of the lattice parameter with the Co^{2+} substitution. Vegard's law predicts the linear change in the lattice parameter for the spinel matrix with the replacement of different ions based on the change in ionic radii of replacing and replaced ions. Since the ionic radius of the Co^{2+} ion (0.65 Å) is smaller than that of the Cu^{2+} ion (0.73 Å), the lattice constant (*a*) is effectively reduced [26]. Also, the presence of La^{3+} ion limits the growth of the crystal structure due to the formation of the *LaFeO$_3$* phase, resulting in a decrease in lattice constant when compared to a pure MNCLF ferrite. The unit cell volume (*V*) is calculated by the equation [27];

$$V = a^3 \qquad (4)$$

The unit cell volume (*V*) decreased from 586.15 Å to 575.43 Å. The hopping lengths L_A and L_B were calculated for the sublattices *A*- and *B*-sites using the following equations [28];

$$L_A = \frac{a\sqrt{3}}{4} \qquad (5)$$

$$L_B = \frac{a\sqrt{2}}{4} \qquad (6)$$

The calculated values of "L_A" and "L_B" for all the as-prepared ferrites are listed in Table 1. The polaron radius (γ) is calculated using equation (7) [10];

$$\gamma = \frac{1}{2} \sqrt[3]{\frac{\pi\, a^3}{576}} \qquad (7)$$

The estimated values of "L_A" and "L_B" along polaron radius (γ) are reported in Table 1 and graphically represented in Fig. 5. The "L_A", "L_B" and "γ" were reduced as the concentration of Co^{2+} was increased, which means that a smaller amount of energy is required for the charge carriers to migrate from one cationic site to another [29]. The "γ" values are smaller than the hopping lengths, which could be attributed to the creation of small polarons [30]. The X-ray (d_X), bulk (d_B) and relative (d_R) densities were calculated by the following relations [29, 31];

$$d_X = \frac{8M}{N_A a^3} \qquad (8)$$

$$d_B = \frac{Mass}{Volume} = \frac{M}{\pi r^2 \times h} \qquad (9)$$

$$d_R = \frac{d_X}{d_B} \qquad (10)$$

where "M" is the molecular weight of the sample and $N_A = 6.02 \times 10^{-23}$ mol^{-1} (Avogadro's number). The density of ferrites plays a vital role in controlling their properties. Table 1 shows the measured bulk density and X-ray density for the investigated ferrite system. With the replacement of Co^{2+} for all of the compositions, an increase in X-ray and bulk densities was observed (Fig. 6). The bulk density is often found to be smaller than the corresponding X-ray density. This may be due to the presence of pores that formed and were established during the sintering process or sample preparation [32]. The relative density was reduced from 120.73 to 115.92 as the doping increased from $x = 0.0$ to $x = 0.5$ (Fig. 6). The percentage of porosity (P%) was estimated using the following relation [33, 34];

$$P\,(\%) = [1 - \frac{d_X}{d_B}] \times 100 \qquad (11)$$

As the doping of Co^{2+} increased, the porosity percentage of the ferrite reduced from 17.17 % to 13.73 %. The formation of the orthorhombic $LaFeO_3$ phase has filled the inter-granular voids, resulting in increased density [28]. Hence, the addition of the Co^{2+} ion is predicted to have a decreasing effect on porosity and as depicted in Fig. 6.

The lattice parameters including the specific surface area (S) [27], packing factor (p) [27], strain (ε) [27] and dislocation density (δ) [27] were calculated by using formulas from equations (12), (13), (14) and (15) and given in Table 1.

$$S = \frac{6000}{\rho_{x \times D}} \quad (12) \qquad\qquad p = \frac{D}{d} \quad (13)$$

$$\varepsilon = \frac{1}{d^2} \quad (14) \qquad\qquad \delta = \frac{1}{D^2} \quad (15)$$

The specific surface area (S) and strain (ε) were increased with the replacement of Co^{2+} with Cu^{2+} in the Co-MNCLF ferrites (Table 1). It is also observed from Table 1 the packing factor (p) was decreased with the substitution of Co^{2+} cation in the lattice sites. The dislocation density (δ) examines the superiority of the as-prepared ferrites. It can be seen in Table 1 the values of "δ" were increased from 4.49×10^{-4} to 13.10×10^{-4} nm^{-2} as the Co^{2+} cation doping changed from $x = 0.0$ to $x = 0.5$.

3.2 Functional group and absorption bands study

FTIR spectra were recorded between 400-4000 cm^{-1} at RT to study the functional group and absorption bands for the as-prepared Co-MNCLF ferrites, as shown in Fig. 7. Oxygen-tetrahedron (Fe–O) and oxygen-octahedron (O–Fe–O) bending vibrations are correlated with higher and lower frequency bands (v_1 and v_2), respectively. The two major frequency bands (higher frequency band (v_1) and lower frequency band (v_2)), lie in the range of $573.80 – 538.65$ cm^{-1} and $470.37 – 405.65$ cm^{-1}, respectively (Table 2). The disparity was observed in v_1 and v_2 with the substitution of Co^{2+} ions. The decreasing trend in v_2 is due to the change in the octahedron's size. The octahedral site is reduced in size as Fe^{3+} and Co^{2+} ions migrate to the octahedral site. Similarly, the remaining Co^{2+} ions occupy the tetrahedral site and induce shrinkage in v_1. The force constants at both tetra- and octahedral sites were calculated by the equation [30];

$$K = 4\pi^2 \, v^2 c^2 m \quad (16)$$

where "c" and "m" represent the speed of light and reduced mass (2.601×10^{-23} g). Table 2 shows that the calculated values of force constants (K_1 and K_2) for tetrahedral and octahedral bands are showing a decreasing trend. It may be due to the decrease in ionic radii of tetrahedral and octahedral sites.

The peaks around 885 cm^{-1} may be due to the bonding of the C–C group [35]. The bands around 1120 cm^{-1} may be due to the remaining C-O vibration [36]. The stretching vibration of the hydroxyl group is attributed to the observed peak at around 3410 cm^{-1}, while the symmetric and asymmetric stretching vibration of atmospheric CO_2 groups is attributed to the other observed peaks at around 1400 and 1600 cm^{-1} [37, 38].

3.3 Raman spectra analysis

Raman spectroscopy is an important tool for discovering substance vibrational and structural properties. Co-MNCLF ferrites have an AB_2O_4 cubic spinel matrix, which corresponds to the ($F d$ -$3 m$) space group and has eight formula units per unit cell. The smallest Bravais cell has just 14 atoms, while the complete unit cell of cubic symmetry has 56. As a result, 42 different vibrational modes are possible. The following optical phonon distribution is predicted by group theory: $5T_{1u}(IR) + A_{1g}(R) + E_g(R) + 3T_{2g}(R)$. The $5T_{1u}$ modes are infrared (*IR*) active modes [18], while the remaining Raman (*R*) active modes ($A_{1g} + E_g + 3T_{2g}$) are due to the motion O^{2-} anions and both the tetrahedral (*A*–) site and octahedral (*B*–) site cations. Raman spectra of Co-MNCLF ferrites were recorded between the range of 200-800 cm^{-1}. A least-square fit with Lorentzian line shape was used to fit the Raman spectra to evaluate the natural frequency, line width, and lattice effect in all ferrites, and their Lorentz fit spectra are depicted in Fig. 8(a-e).

The values of active Raman modes are reported in Table 3. The Raman mode "A_{1g}" lies in the range 677 – 690 cm^{-1} represents the symmetric stretching of the bond that exists between Fe^{3+}/Metal–O^{2-} in the tetrahedral (*A*–) site. The Raman modes "$T_{2g}(3)$", "$T_{2g}(2)$" and "E_g" lie in the range 548 – 633 cm^{-1}, 468 – 487 cm^{-1}, and 328 – 391 cm^{-1}, respectively originating in the octahedral (*B*–) site due to anti-symmetric stretching of metal-oxygen bonds. Finally, the translation movement of the MO_4 tetrahedral units is associated with the $T_{2g}(1)$ mode, lying in the range of 301–322 cm^{-1}.

3.4 UV-vis spectroscopy analysis

The optical band gap (E_g) of materials that are good candidates for optoelectronic applications is the most significant property. The absorption coefficient (α) for Co-MNCLF ferrites was calculated by using the following equation [10];

$$\alpha = 2.303 \frac{log(A)}{l} \tag{17}$$

where 'A' and '*l*' represent absorbance and the path length of light in which absorbance takes place, respectively. Tauc's plots (Fig. 9(a-e)) were used to determine the optical band gap of Co-MNCLF ferrites and the following relation was employed as [10];

$$\alpha h v = B(h v - Eg)^n \tag{18}$$

where '*h*' is Planck constant, '*v*' is the frequency, and '*B*' is the transition probability dependence constant. "*n*" is constant, having value 1/2 or 2. It was found that the optical band gap (E_g) increased from 0.85 eV to 1.33 eV for $x = 0.0$ to $x = 0.25$ and then observed optical band gap was 1.15 eV and 1.46 eV for $x = 0.375$ to $x = 0.5$, respectively, as shown in Fig. 9(a-

e). It is because Co^{2+} is less conductive than Cu^{2+} and also the existence of La^{3+} formed *LaFeO₃* phase at grain boundary is responsible for this trend.

3.5 I-V measurement analysis

Let us now turn to the impact of Co^{2+} doping on the electrical characteristics of the as-prepared ferrites. Fig. 10 illustrates the temperature dependence of resistivity (ρ) for the Co-MNCLF ferrites in the temperature range 323–673 K. Fig. 10 also reveals the Arrhenius plots i.e., $10^3/T$ as a function of the log of resistivity. A kink occurs in the Arrhenius plots in the range 393 – 433 K (Table 4) for all the ferrites and represents Curie temperature (T_C). The kink of $10^3/T$ values change with the dopant concentration and the $x = 0.25$ sample has a smaller value than other samples. It may be due to a change in dopant concentration and the development of the *LaFeO₃* phase at grain boundaries. It has two regions separated by the black dotted line (Fig. 10). The region before the Curie temperature (T_C) is associated as a ferromagnetic region, while the region above Curie temperature (T_C) is called the Paramagnetic region. The resistivity (ρ) increases in the Ferro region and then drops continuously in the para region with increasing temperature for all ferrites. The activation energy (E_a) is calculated by taking the slope of Arrhenius plots using relation [27];

$$E_a = 2.303 \times k_B \times 10^3 \times slope \ (eV) \tag{19}$$

where "k_B" represents Boltzmann constant (8.602×10^{-5} eV/K). The activation energy (ΔE) of the Co-MNCLF ferrites are given in Table 4 and observed that the maximum "E_a" was 0.8625 eV for sample concentration $x = 0.25$ (Fig. 11). The concentration of charge carriers (η) was estimated using equation [27];
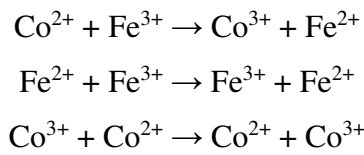
$$\eta = \frac{N_A d_B P_{Fe}}{M} \tag{20}$$

where "P_{Fe}" is the number of Fe atoms in Co-MNCLF ferrites and the calculated values of "η" are reported in Table 4. The drift mobility (μ_d) of Co-MNCLF ferrites were determined *via* the following equation [27];

$$\mu_d = \frac{1}{\eta e \rho} \tag{21}$$

where 'e' charge of an electron ($4.8032451 \times 10^{-10}$ esu) [11]. The calculated values of "μ_d" were decreased from 1.217×10^{-14} to 1.108×10^{-14} cm²/Vs, as the doping of Co^{2+} increased from $x = 0.0$ to $x = 0.5$ at 323 K (Fig. 11). It was observed from Fig. 2 that *LaFeO₃* phase intensity increased with the substitution of dopant ions along with La^{3+} ions. Therefore, the drift mobility was reduced when compared with the pure MNCLF sample (as seen in Fig. 11). It was also observed from Fig. 11 that the maximum Curie temperature was 433 K at $x = 0.25$.

8

Fig. 12(a-c) indicates the plots of Co^{2+} concentration (x) *versus* (a) log of resistivity (ρ) at low temperature [323 K – 413 K] (b) log of resistivity (ρ) at medium temperature [423 K – 493 K] (c) log of resistivity (ρ) at high temperature [503 K – 673 K]. It was found from Fig. 12(a) that the resistivity (ρ) was minimum for Co^{2+} concentration $x = 0.25$ except at 323 K and Fig. 12(b-c) revealed that the resistivity (ρ) was maximum for Co^{2+} doping $x = 0.25$ at higher temperatures. It was also observed from Fig. 12(a-c) that at low temperature the resistivity (ρ) increased when the temperature increased from 323 K to 413 K. Electron hopping between ions of a similar element with different valence states is responsible for resistivity. In other words, a change in resistivity is caused by cationic distribution in the spinel matrix. In our case, one of the following processes governs the existence of ions with several valence states:

$$Co^{2+} + Fe^{3+} \rightarrow Co^{3+} + Fe^{2+}$$
$$Fe^{2+} + Fe^{3+} \rightarrow Fe^{3+} + Fe^{2+}$$
$$Co^{3+} + Co^{2+} \rightarrow Co^{2+} + Co^{3+}$$

It was also observed from Fig. 12(b-c) that the resistivity (ρ) was reduced as the temperature increased in the medium (423 K – 493 K) and high (503 K –673 K) temperature range. The decrease in resistivity with rising temperature due to high lattice vibrations at high temperatures could be explained by the maximum transfer of electrons, causing the ions to come closer for easier electron transfer and thus inducing conduction.

The temperature coefficient of resistance (TCR) is extremely valuable for assessing the sensitivity of infrared detectors (IR) used in night vision bolometers [39]. The TCR percentage was calculated using the following relation [40];

$$TCR = \frac{1}{\rho}\left[\frac{d\rho}{dT}\right] \times 100 \qquad (20)$$

Where "T" is temperature and "ρ" is resistivity. The TCR% data of Co-MNCLF as a function of temperature is shown in Fig. 13. The peak position of the Fig. 13 revealed that TCR% values are −3.01%/K at 433 K, −6.97%/K at 433 K, −2.66%/K at 513 K, −5.54%/K at 433 K and −4.71%/K at 443 K for $x = 0.0$, $x = 0.125$, $x = 0.25$, $x = 0.375$ and $x = 0.5$ sample, respectively. It may be due to the existence of La^{3+} ions which formed the *LaFeO₃* phase at the grain boundaries along with the dopant ions. Sintering temperature and time are two elements that could also affect peak TCR% value [41]. These findings indicate that Co-MNCLF ferrites could be employed in bolometric devices, which is encouraging.

Fig. 14(a-c) revealed the plots of Co^{2+} concentration (x) *versus* TCR % at different temperatures. It can be seen in Fig. 14(a) that the TCR % is positive between the temperature range 323 K – 393 K and has a maximum value at Co^{2+} doping $x = 0.375$. It was also found

9

from Fig. 14(a) that the values of TCR % reduced as the temperature increased from 323 K to 393 K. It can be shown in Fig. 14(b) that the values of TCR % between the temperature range 403 K – 493 K and has different TCR % at different temperatures as well as different Co^{2+} concentration (x). Fig. 14(c) revealed that the TCR % was increased with increasing the temperature from 503 K to 573 K. Fig. 14(d) indicated the TCR % at 623 K and 673 K for different Co^{2+} ion concentrations.

3.6 Dielectric analysis

At room temperature, the dielectric constant including real (ε') and imaginary (ε'') part as a function of frequency were measured and illustrated in Figs. 15(a) and 15(b), respectively. With an increase in frequency, the dielectric behavior, both real and imaginary parts of the dielectric constant, exhibits a declining tendency. In the low-frequency area, the dielectric behavior dispersion is quite sharp, whereas, in the high-frequency region, it is constant. The polarization caused by changes in space charge polarization and cation different valence states is thought to be the cause of the behavior. The difficulty of the electric dipoles to follow fast changes in the field causes the dielectric constant to behave nearly frequency-independent at higher frequencies. Because the electronic and atomic polarization is mostly unaltered at these frequencies, the frequency dispersion seen in this work is considered to be attributable to interfacial polarization [42, 43]. Two-layer model, the observed behavior may be described using Maxwell-Wagner interfacial polarization, which agrees with the phenomenological theory of Koop's. Koop's theory suggests that the materials are made up of two layers: one with good conducting grains and the other with extremely resistive grain boundaries. The electrons are reached by a hopping mechanism to the insulating grain boundaries, where they concentrate due to the structure's resistivity. This charge accumulation under the impact of the field leads to a rise in interfacial polarization and, as a result, a larger dielectric constant value at low frequencies. Because the charge carrier's inhomogeneous dielectric matrix takes a certain amount of time to align themselves along the direction of the field, the dielectric constant naturally reduces as the frequency increases. In the low-frequency area, between two Fe sites hopping of charges, i.e., Fe^{3+} and Fe^{2+}, synchronize with the field, but in the larger frequency region, this synchronization fails and the field lags, resulting in an independent frequency like a response [42, 43]. Furthermore, at high frequencies, the dielectric constant is insensitive to the heterogeneity impact, and grain boundary resistivity is greater, which slows down the hopping process and lowers the dielectric constant value. It was also observed from Figs. 15(a) and 15(b) that the dielectric constants first reduced and then increased with the substitution of

Co^{2+} ions at the lattice sites. For Co^{2+} doping $x = 0.125$, has minimum dielectric constants. It has a maximum value for $x = 0.25$ at low frequency and for $x = 0.375$ at high frequency.

The dielectric loss factor known as tangent loss (tan δ) is a significant component of total core loss in ferrites. The structural homogeneity, the quantity of Fe^{2+} ions, and synthesis variables including sintering time, temperature, and heat all influence the magnitude of the loss tangent. The fluctuation of "tan δ" as a function of "log f" is shown in Fig. 15(c). Because charge hopping between Fe^{2+} and Fe^{3+} can only follow the frequency of the field up to a certain point, the "tan δ" drops as the frequency of the field increases. There is a close link between ferrite's conduction mechanism and their dielectric properties. The resistivity of the grain boundaries increases as the frequency increases, decreasing the charge exchange mechanism and therefore lowering the dielectric loss value [44]. The "tan δ" follows the same pattern as the dielectric constant, first reduced and then increased as the Co^{2+} doping increases. For $x = 0.125$ concentration, the tangent loss has minimum value.

Ferrite's electrical characteristics are comparable to that of semiconductors and are an important factor in determining their use in electronic devices [42]. At room temperature, the *ac* conductivity (σ_{ac}) of Co-MNCLF ferrites was measured as a function of frequency, depicted in Fig. 15(d). It was found from Fig. 15(d) that the "σ_{ac}" increased with increment in the applied frequency. It may be due to the hopping frequency between Fe^{2+} and Fe^{3+} ions rising as the field frequency increases, therefore ac-conductivity increased.

At room temperature, Fig. 16(a) depicts the change of the real part of impedance (Z') with frequency for all the ferrites. With increased frequency, the value of "Z'" is found to rapidly declined and the reduction in "Z'" implies that conduction is rising as frequency increases. At lower frequencies, the value of "Z'" was observed maximum for Co^{2+} doping $x = 0.125$ and minimum for $x = 0.375$. The higher "Z'" values at lower frequencies indicate more polarization and this is due to the presence of all types of polarization at lower frequencies. It was also important to note that the values of "Z'" for all the ferrites coincide around 1 MHz. The lower values of "Z'" for all the ferrites at higher frequencies is due to space charge polarization that exists at the homogenous phase boundaries in ferrites under externally applied fields. Fig. 16(b) depicts the change of imaginary part of impedance (Z'') with frequency for all the ferrites. It is clear from Fig. 16(b) that the values of "Z''" also reduced with increasing the frequency and the minimum values of "Z''" was found for Co^{2+} concentration $x = 0.125$.

The Cole-Cole (CC) plots, "Z'" against "Z''", is shown in Fig. 17(a-e). For the Co-MNCLF ferrites, two semicircles were observed. The semicircle at lower frequency indicates

the total grain resistance and grain boundaries, whereas the semicircle at higher frequency simply represents grain resistance. Starting from the origin, all Co^{2+} replaced compositions display a single semicircular arc and second semicircles in the CC plots suggest that the materials only have a grain influence on the conductivity mechanism [42]. It was observed that the diameter of the semicircle increased with the Co^{2+} ions doping up to $x = 0.375$ and then decreased. The resistance of the grain is corresponding to the diameter of the CC plots semicircle [42].

The Q factor value is the reciprocal of the dissipation factor (tan δ) [45]. The log of frequency *versus* Q-factor plots is seen in Fig. 18. It was noted that the value of Q is larger at a higher frequency above 1 MHz. As a result, the resonance frequency of more than 1 MHz and the excellent quality factor indicate that Co-MNCLF ferrites may be used in high-frequency multilayers and resonance circuits.

4 Conclusions

For Co-MNCLF ferrites synthesized by employing the sol-gel auto-combustion method, it was observed that as Co^{2+} doping (x) increases from $x = 0.0$ to $x = 0.5$, the lattice constant (a) was reduced, while the replacement of Co^{2+} for all of the compositions, an increasing trend in X-ray and bulk densities was found. The disparity was found in υ_1 and υ_2 with the substitution of Co^{2+} ions. The Raman mode "A_{1g}" lies in the range $677 - 690$ cm^{-1} while Raman modes "T_{2g} (3)", "T_{2g} (2)" and "E_g" lie in the range $548 - 633$ cm^{-1}, $468 - 487$ cm^{-1}, and $328 - 391$ cm^{-1}, respectively. Moreover, the T_{2g} (1) mode lies in the range of $301–322$ cm^{-1}. The optical band gap (E_g) was minimum (0.85 eV) for $x = 0.0$ and maximum (1.46 eV) for $x = 0.5$. The resistivity (ρ) was reduced as the temperature increased in the medium (423 K – 493 K) and high (503 K –673 K) temperature range. The peak position of the temperature *versus* TCR% revealed that the TCR% values are -3.01%/K at 433 K, -6.97%/K at 433 K, -2.66%/K at 513 K, -5.54%/K at 433 K and -4.71%/K at 443 K for $x = 0.0$, $x = 0.125$, $x = 0.25$, $x = 0.375$ and $x = 0.5$ sample. The dielectric constants first reduced and then increased with the substitution of Co^{2+} ions at the lattice sites. At lower frequencies, the value of "Z'" was maximum for Co^{2+} doping $x = 0.125$ and minimum for $x = 0.375$. The high optical band gap, resistivity, and TCR are valuable for the promising infrared detector (IR) for night vision bolometers and optoelectrical. Therefore, the sample with Co^{2+} concentration $x = 0.125$ has exhibited the highest temperature coefficient of resistance (-6.97%/K at 433 K) among other samples that indicated that it might be a promising infrared detector (IR) for night vision bolometers.

References

[1] K. Hussain, N. Amin, M.I. Arshad, Evaluation of structural, optical, dielectric, electrical, and magnetic properties of Ce^{3+} doped $Cu_{0.5}Cd_{0.25}Co_{0.25}Fe_{2-x}O_4$ spinel nano-ferrites, Ceramics International, 47 (2021) 3401-3410.

[2] M.A. Aswad, F.A. Mutlak, M.S. Jabir, S.K. Abdulridha, A.F. Ahmed, U.M. Nayef, Laser assisted hydrothermal synthesis of magnetic ferrite nanoparticles for biomedical applications, Journal of Physics: Conference Series, IOP Publishing, 2021, pp. 012030.

[3] K. Orikawa, S. Ogasawara, M. Takemoto, J.i. Itoh, A 2.5 MHz High-Frequency Output Inverter Based on Frequency Multiplying Technique with a Multi-Core Transformer using Mn-Zn Ferrite Materials, IEEJ Journal of Industry Applications, 10 (2021) 370-376.

[4] M. Ghanbari, F. Davar, A.E. Shalan, Effect of rosemary extract on the microstructure, phase evolution, and magnetic behavior of cobalt ferrite nanoparticles and its application on anti-cancer drug delivery, Ceramics International, 47 (2021) 9409-9417.

[5] I.B.T. da Silva, A.G. D'Assunção, J.B.L. de Oliveira, S.M. de Holanda, C.H.N. Cordeiro, Design and analysis of nickel ferrite resonator antenna for C band applications, Microwave Optical Technology Letters, 63 (2021) 1781-1785.

[6] I. Vedernikova, A. Koval, A. Dedusenko, Synthesis of nanoparticles zinc ferum (ii) ferrites for pharmaceutical means with magnetically properties, Farmatsevtychnyi zhurnal, (2011) 78-82.

[7] C. Virlan, F. Tudorache, A. Pui, Tertiary NiCuZn ferrites for improved humidity sensors: a systematic study, Arabian Journal of Chemistry, 13 (2020) 2066-2075.

[8] P. Akhtar, M.N. Akhtar, M. Baqir, A. Ahmad, M.U. Khallidoon, M. Farhan, M.A. Khan, Structural and magnetic evaluations of rare-earths (Tb, Pr, Ce, Gd, Y)-doped spinel ferrites for high frequency and switching applications, Journal of Materials Science: Materials in Electronics, 32 (2021) 7692-7703.

[9] M. Malarvizhi, S. Meyvel, M. Sandhiya, M. Sathish, M. Dakshana, P. Sathya, D. Thillaikkarasi, S. Karthikeyan, Design and fabrication of cobalt and nickel ferrites based flexible electrodes for high-performance energy storage applications, Inorganic Chemistry Communications, 123 (2021) 108344.

[10] A. Aslam, A.U. Rehman, N. Amin, M.A. un Nabi, Q. ul ain Abdullah, N. Morley, M.I. Arshad, H.T. Ali, M. Yusuf, Z. Latif, Lanthanum doped $Zn_{0.5}Co_{0.5}La_xFe_{2-x}O_4$ spinel ferrites synthesized via co-precipitation route to evaluate structural, vibrational, electrical, optical, dielectric, and thermoelectric properties, Journal of Physics and Chemistry of Solids, 154 (2021) 110080.

[11] A. Aslam, A. Razzaq, S. Naz, N. Amin, M.I. Arshad, M.A.U. Nabi, A. Nawaz, K. Mahmood, A. Bibi, F. Iqbal, Impact of Lanthanum-Doping on the Physical and Electrical Properties of Cobalt Ferrites, Journal of Superconductivity and Novel Magnetism, (2021) 1-10.

[12] I. ALIa, N. Amin, A. REHMAN, M. Akhtar, M. Fatima, K. Mahmood, A. ALIa, G. Mustafa, M. Hasan, A. Bibi, ELECTRICAL AND MAGNETIC PROPERTIES OF $BaCo_xCd_{2-x}Fe_{16}O_{27}$ W-TYPE HEXAFERRITES ($0\leq x\leq 0.5$), Digest Journal of Nanomaterials Biostructures, 15 (2020).

[13] N. Amin, M. Akhtar, M. Sabir, K. Mahmood, A. ALIa, G. Mustafa, M. Hasan, A. Bibi, M. Iqbal, F. Iqbal, SYNTHESIS, STRUCTURAL AND OPTICAL PROPERTIES OF Zn-

SUBSTITUTED Co W-FERRITES BY COPRECIPITATION METHOD, Journal of Ovonic Research, 16 (2020) 11-19.

[14] H.T. Ali, M. Ramzan, M.I. Arshad, N.A. Morley, M.H. Abbas, M. Yusuf, A.U. Rehman, K. Mahmood, A. Ali, N. Amin, Tailoring the optical, and magnetic properties of La-BaM hexaferrites by Ni substitution, Chinese Physics B, (2021).

[15] A.U. Rehman, N. Morley, N. Amin, M.I. Arshad, M.A. un Nabi, K. Mahmood, A. Ali, A. Aslam, A. Bibi, M.Z. Iqbal, Controllable synthesis of La^{3+} doped $Zn_{0.5}Co_{0.25}Cu_{0.25}Fe_{2-x}La_xO_4$ (x= 0.0, 0.0125, 0.025, 0.0375, 0.05) nano-ferrites by sol-gel auto-combustion route, Ceramics International, 46 (2020) 29297-29308.

[16] A.U. Rehman, N. Amin, M.B. Tahir, M.A. un Nabi, N. Morley, M. Alzaid, M. Amami, M. Akhtar, M.I. Arshad, Evaluation of spectral, optoelectrical, dielectric, magnetic, and morphological properties of RE^{3+} (La^{3+}, and Ce^{3+}) and Co^{2+} co-doped $Zn_{0.75}Cu_{0.25}Fe_2O_4$ ferrites, Materials Chemistry and Physics, (2021) 125301.

[17] A. Aslam, A.U. Rehman, N. Amin, M. Amami, M. Nabi, H. Alrobei, M. Asghar, N. Morley, M. Akhtar, M.I. Arshad, Sol–Gel Auto-combustion Preparation of $M^{2+}= Mg^{2+}$, Mn^{2+}, Cd^{2+} Substituted $M_{0.25}Ni_{0.15}Cu_{0.25}Co_{0.35}Fe_2O_4$ Ferrites and Their Characterizations, Journal of Superconductivity and Novel Magnetism, (2021) 1-11.

[18] L. Zhang, Y. Wang, B. Liu, J. Wang, G. Han, Y. Zhang, Characterization and property of magnetic ferrite ceramics with interesting multilayer structure prepared by solid-state reaction, Ceramics International, 47 (2021) 10927-10939.

[19] D. Jnaneshwara, D. Avadhani, B.D. Prasad, H. Nagabhushana, B. Nagabhushana, S. Sharma, S. Prashantha, C. Shivakumara, Role of Cu^{2+} ions substitution in magnetic and conductivity behavior of nano-$CoFe_2O_4$, Spectrochimica Acta Part A: Molecular and Biomolecular Spectroscopy, 132 (2014) 256-262.

[20] A. Samavati, M. Mustafa, A. Ismail, M. Othman, M. Rahman, Copper-substituted cobalt ferrite nanoparticles: structural, optical and antibacterial properties, Materials Express, 6 (2016) 473-482.

[21] M. Pourzaki, R. Kavkhani, A. Kianvash, A. Hajalilou, Structure, magnetic and transmission characteristics of the Co substituted Mg ferrites synthesized via a standard ceramic route, Ceramics International, 45 (2019) 5710-5716.

[22] I. Ahmad, T. Abbas, M. Islam, A. Maqsood, Study of cation distribution for Cu–Co nanoferrites synthesized by the sol–gel method, Ceramics International, 39 (2013) 6735-6741.

[23] K. Pubby, S. Meena, S. Yusuf, S.B. Narang, Cobalt substituted nickel ferrites via Pechini's sol–gel citrate route: X-band electromagnetic characterization, Journal of Magnetism and Magnetic Materials, 466 (2018) 430-445.

[24] K.K. Bharathi, C. Ramana, Improved electrical and dielectric properties of La-doped Co ferrite, Journal of Materials Research, 26 (2011) 584-591.

[25] M.A. Maksoud, A. El-Ghandour, A. Ashour, M. Atta, S. Abdelhaleem, A.H. El-Hanbaly, R.A. Fahim, S.M. Kassem, M. Shalaby, A. Awed, La^{3+} doped $LiCo_{0.25}Zn_{0.25}Fe_2O_4$ spinel ferrite nanocrystals: Insights on structural, optical and magnetic properties, Journal of Rare Earths, 39 (2021) 75-82.

[26] A. Azam, Microwave assisted synthesis and characterization of Co doped Cu ferrite nanoparticles, Journal of alloys and compounds, 540 (2012) 145-153.

[27] K. Hussain, A. Bibi, F. Jabeen, N. Amin, K. Mahmood, A. Ali, M.Z. Iqbal, M. Arshad, Study of structural, optical, electrical and magnetic properties of Cu^{2+} doped $Zn_{0.4}Co_{0.6-x}Ce_{0.1}Fe_{1.9}O_4$ spinel ferrites, Physica B: Condensed Matter, 584 (2020) 412078.

[28] M.A.U. Nabi, M. Moin, M. Hasan, M. Arshad, A. Bibi, N. Amin, K. Mahmood, S. Ali, Study of Electrical Transport Properties of Cadmium-Doped Zn–Mn Soft Ferrites by Co-precipitation Method, Journal of Superconductivity and Novel Magnetism, (2020) 1-10.

[29] N. Amin, M.S.U. Hasan, Z. Majeed, Z. Latif, M.A. un Nabi, K. Mahmood, A. Ali, K. Mehmood, M. Fatima, M. Akhtar, Structural, electrical, optical and dielectric properties of yttrium substituted cadmium ferrites prepared by Co-Precipitation method, Ceramics International, 46 (2020) 20798-20809.

[30] T. Tatarchuk, N. Paliychuk, M. Pacia, W. Kaspera, W. Macyk, A. Kotarba, B.F. Bogacz, A.T. Pędziwiatr, I. Mironyuk, R. Gargula, Structure–redox reactivity relationships in $Co_{1-x}Zn_xFe_2O_4$: the role of stoichiometry, New Journal of Chemistry, 43 (2019) 3038-3049.

[31] R. Zakir, S.S. Iqbal, A.U. Rehman, S. Nosheen, T.S. Ahmad, N. Ehsan, F. Inam, Spectral, electrical, and dielectric characterization of Ce-doped Co-Mg-Cd spinel nano-ferrites synthesized by the sol-gel auto combustion method, Ceramics International, 47 (2021) 28575-28583.

[32] M. Hossain, M. Khan, A. Nahar, M. Ali, M. Matin, S. Hoque, M. Hakim, A. Jamil, Tailoring the properties of Ni-Zn-Co ferrites by Gd^{3+} substitution, Journal of Magnetism and Magnetic Materials, 497 (2020) 165978.

[33] A. Manzoor, M.A. Khan, W. Kuch, Correlation between ferromagnetic resonance and densification of RE substituted polycrystalline ferrites, Ceramics International, 44 (2018) 13328-13334.

[34] N. Amin, A. Razaq, A.U. Rehman, K. Hussain, M. Nabi, N. Morley, M. Amami, A. Bibi, M.I. Arshad, K. Mahmood, Transport Properties of Ce-Doped Cd Ferrites $CdFe_{2-x}Ce_xO_4$, Journal of Superconductivity and Novel Magnetism, (2021) 1-11.

[35] M. Goodarz Naseri, E.B. Saion, H. Abbastabar Ahangar, A.H. Shaari, M. Hashim, Simple synthesis and characterization of cobalt ferrite nanoparticles by a thermal treatment method, Journal of Nanomaterials, 2010 (2010).

[36] W. Zhang, A. Sun, X. Zhao, N. Suo, L. Yu, Z. Zuo, Structural and magnetic properties of La^{3+} ion doped Ni–Cu–Co nano ferrites prepared by sol–gel auto-combustion method, Journal of Sol-Gel Science and Technology, 90 (2019) 599-610.

[37] H. Kumar, J.P. Singh, R. Srivastava, P. Negi, H. Agrawal, K. Asokan, FTIR and electrical study of dysprosium doped cobalt ferrite nanoparticles, Journal of Nanoscience, 2014 (2014).

[38] S. Nithiyanantham, S. Viviliya, S. Anandhan, S. Mahalakshmi, Synthesis and Characterization of Cobalt Ferrite through Co-Precipitation Technique, Letters in Applied NanoBioScience 10 (2020) 1871 - 1876.

[39] H. Chouaya, M. Smari, I. Walha, E. Dhahri, M. Graça, M. Valente, The effect of bismuth on the structure, magnetic and electric properties of Co_2MnO_4 spinel multiferroic, Journal of Magnetism and Magnetic Materials, 451 (2018) 344-350.

[40] R. Hamdi, A. Tozri, M. Smari, E. Dhahri, L. Bessais, Structural, magnetic, magnetocaloric and electrical studies of $Dy_{0.5}(Sr_{1-x}Ca_x)_{0.5}MnO_3$ manganites, Journal of Magnetism and Magnetic Materials, 444 (2017) 270-279.

[41] J. Massoudi, M. Smari, K. Nouri, E. Dhahri, K. Khirouni, S. Bertaina, L. Bessais, Magnetic and spectroscopic properties of Ni–Zn–Al ferrite spinel: from the nanoscale to microscale, RSC Advances, 10 (2020) 34556-34580.

[42] K.M. Batoo, G. Kumar, Y. Yang, Y. Al-Douri, M. Singh, R.B. Jotania, A. Imran, Structural, morphological and electrical properties of Cd^{2+} doped $MgFe_{2-x}O_4$ ferrite nanoparticles, Journal of Alloys and Compounds, 726 (2017) 179-186.

[43] M.A. Iqbal, M. Islam, I. Ali, I. Sadiq, I. Ali, High frequency dielectric properties of Eu+3-substituted Li–Mg ferrites synthesized by sol–gel auto-combustion method, Journal of alloys and compounds, 586 (2014) 404-410.

[44] V. Manikandan, V. Kuncser, B. Vasile, S. Kavita, S. Vigneselvan, R. Mane, Enhancement in magnetic and dielectric properties of the ruthenium-doped copper ferrite ($Ru-CuFe_2O_4$) nanoparticles, Journal of Magnetism and Magnetic Materials, 476 (2019) 18-23.

[45] M. Sharif, J. Jacob, M. Javed, A. Manzoor, K. Mahmood, M.A. Khan, Impact of Co and Mn substitution on structural and dielectric properties of lithium soft ferrites, Physica B: Condensed Matter, 567 (2019) 45-50.
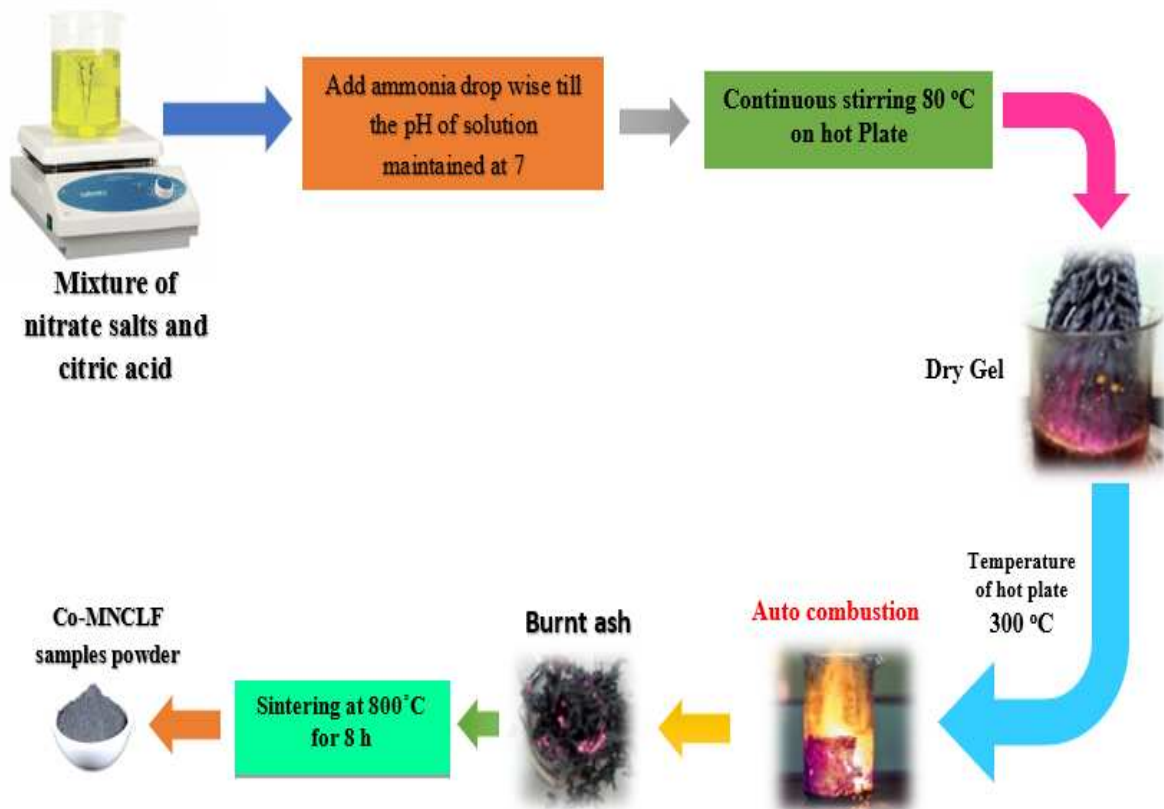
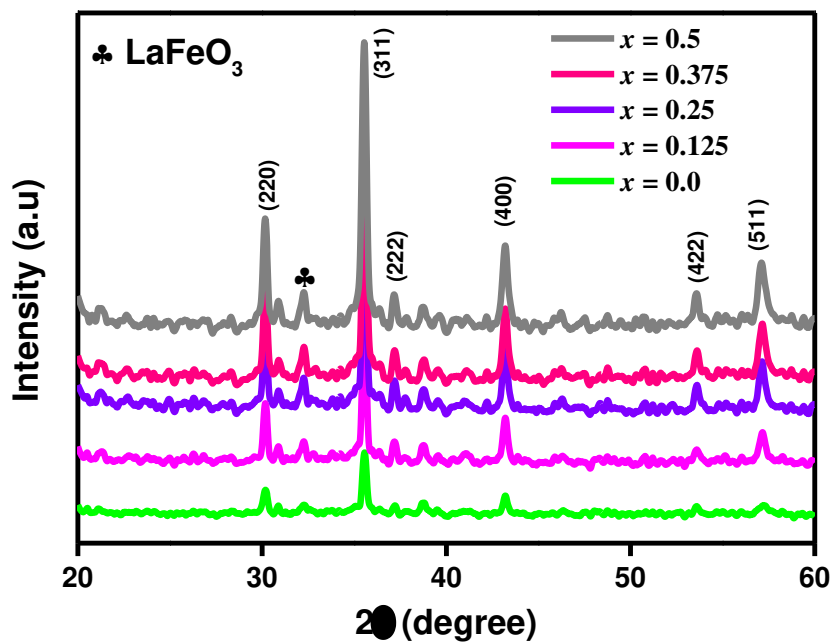**Fig. 1 Step by step ferrites preparation process**

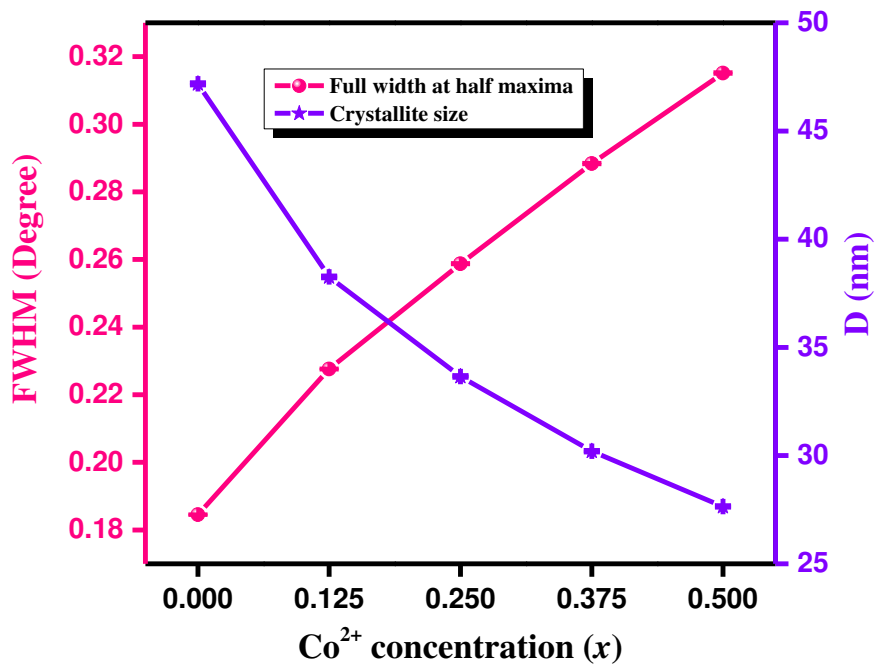**Fig. 2** XRD spectra for Co-MNCLF ferrites (JCPDS card no: 34-0425)

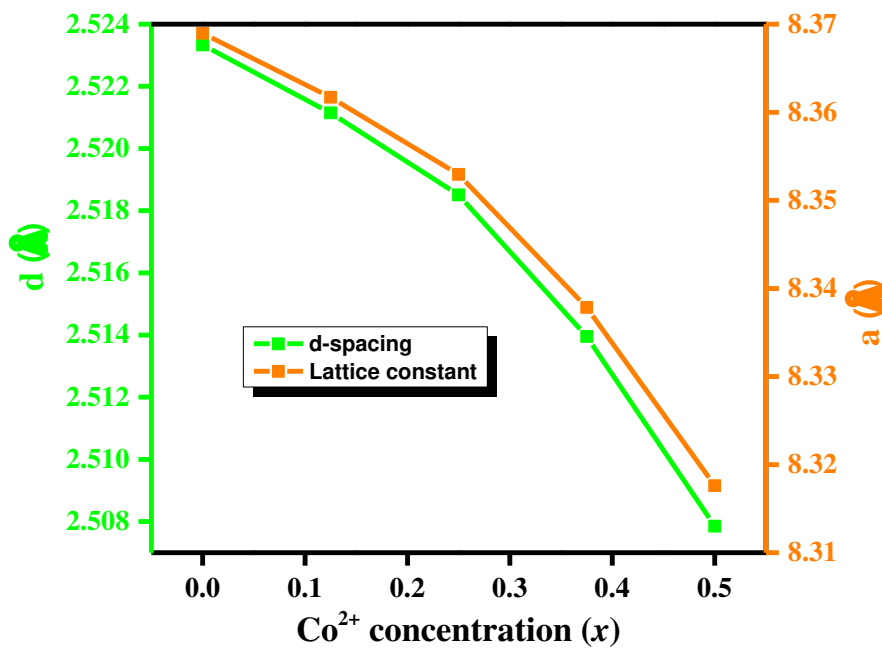**Fig. 3** Co^{2+} concentration *versus* FWHM and crystallite size

Fig. 4 Co^{2+} concentration *versus* d-spacing and lattice constant
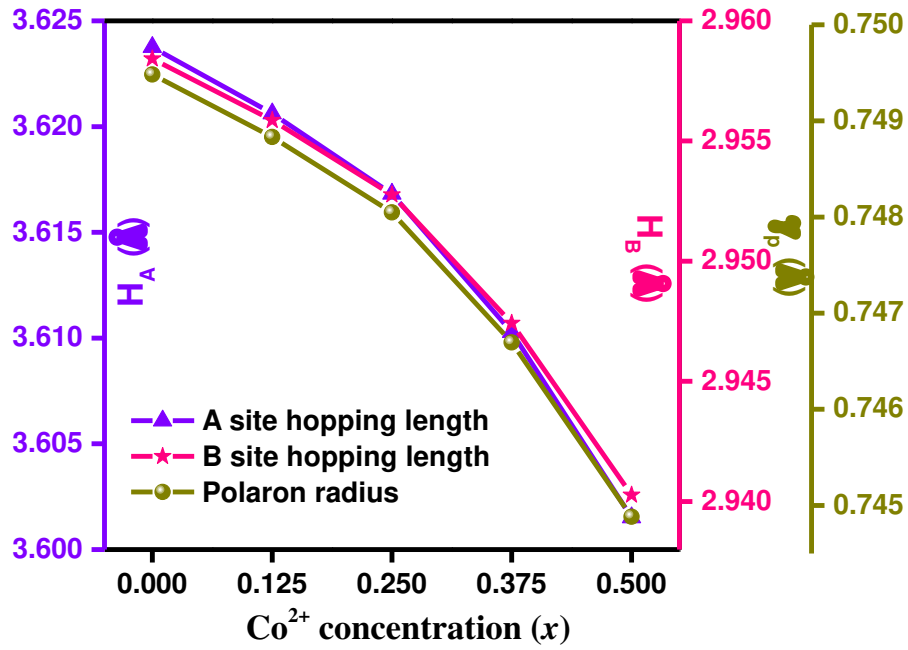
Fig. 5 Co^{2+} concentration *versus* hopping length at *A*- and *B*- sites along with polaron radius
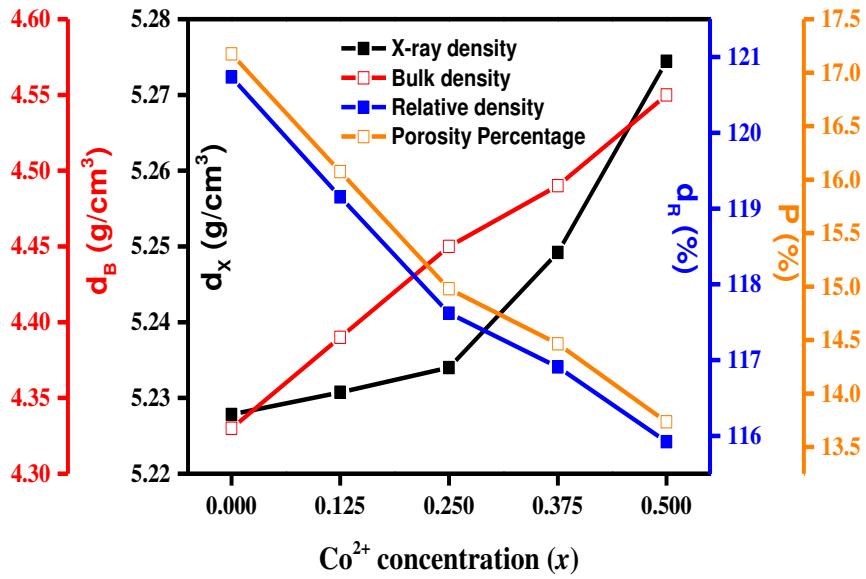
Fig. 6 Co^{2+} concentration *versus* X-ray, bulk and relative densities along with porosity percentage
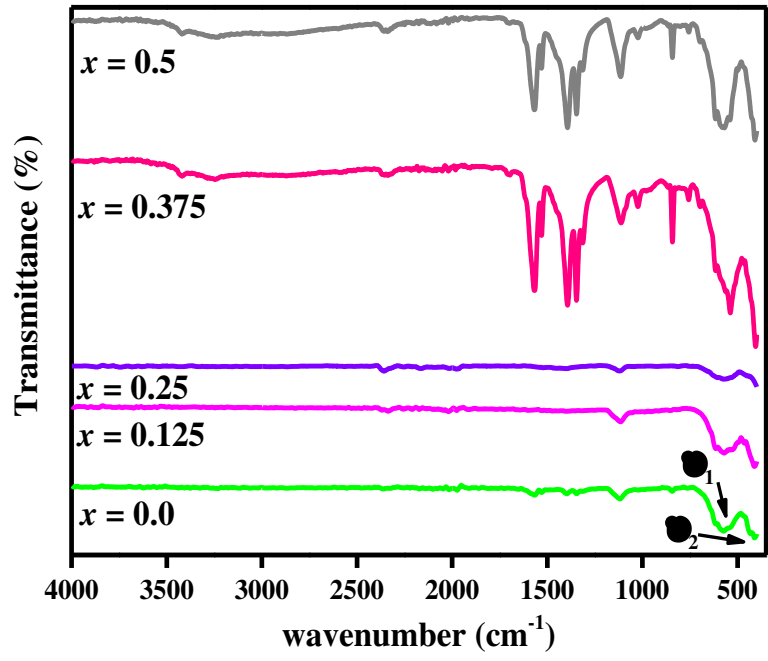
Fig. 7 FTIR spectra for the Co-MNCLF ferrites
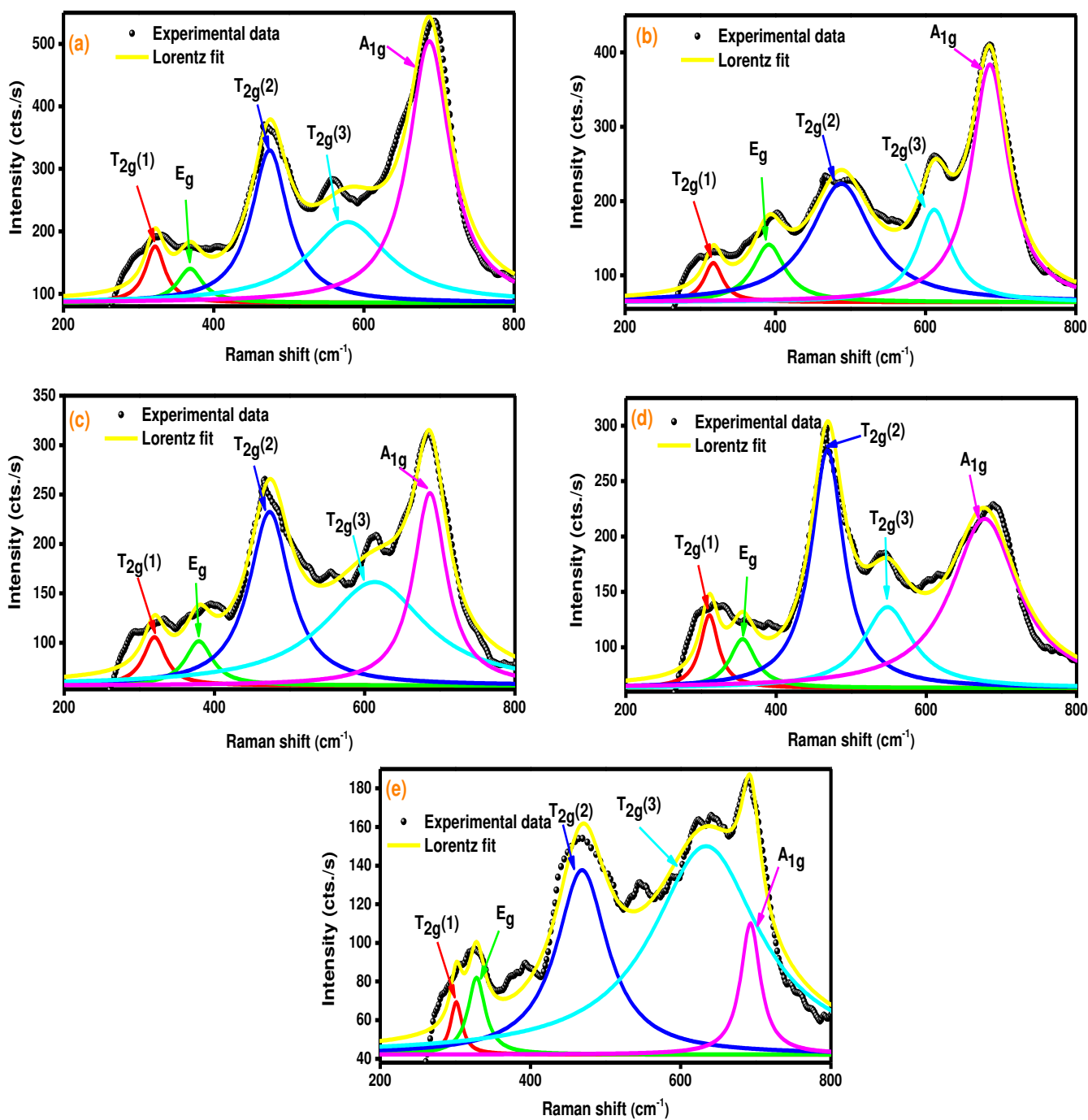
Fig. 8(a-e) Raman spectra of Co-MNCLF ferrites
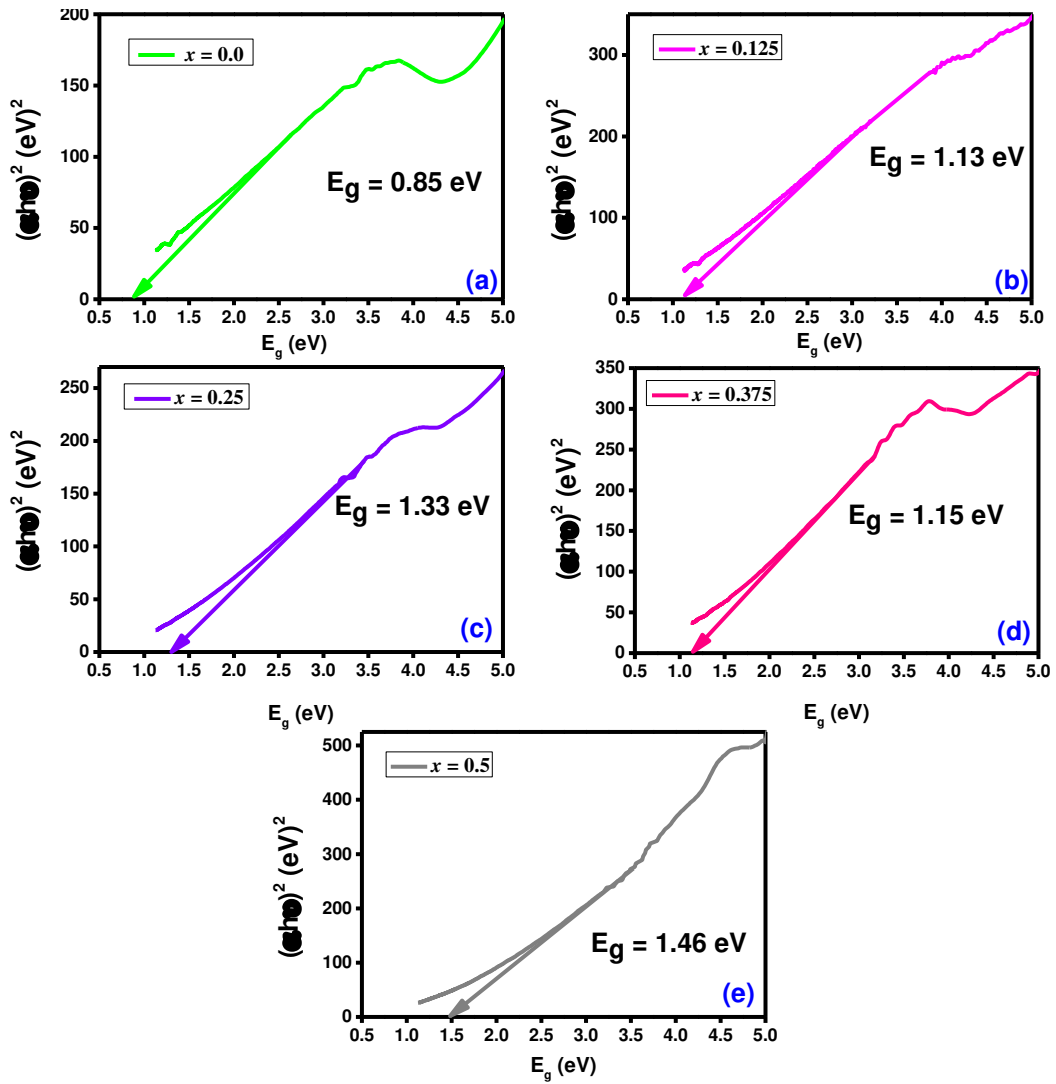
Fig. 9(a-e) Tauc's plots for all the ferrites
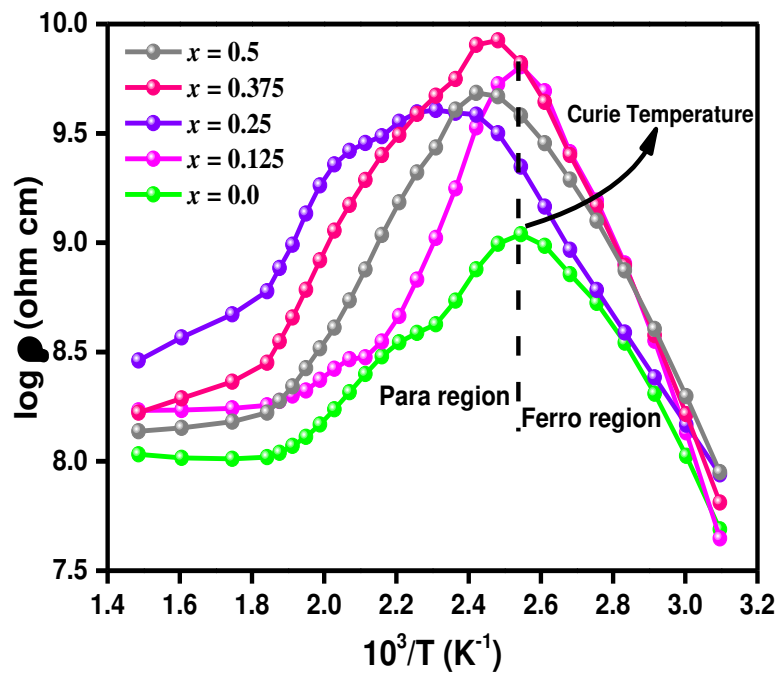
Fig. 10 Arrhenius plots for Co-MNCLF ferrites

22
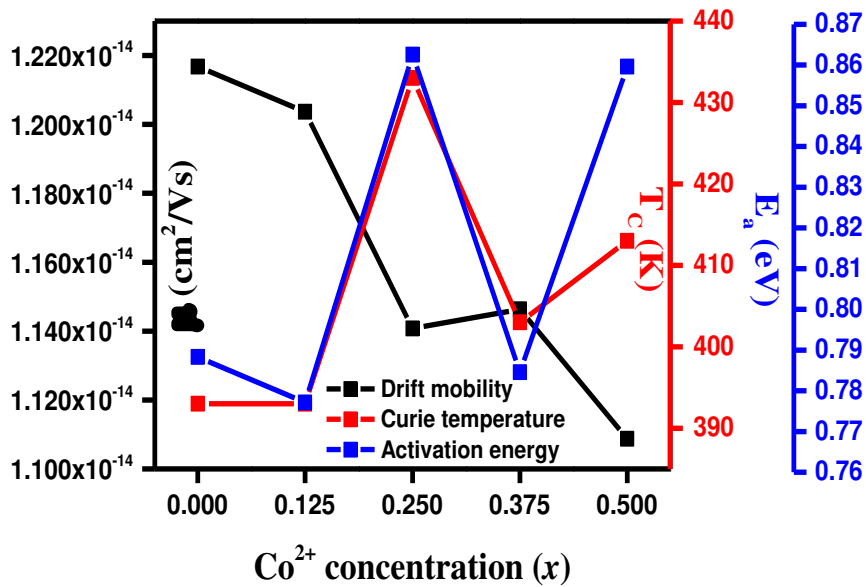
Fig. 11 Co^{2+} concentration *versus* drift mobility, Curie temperature and activation energy
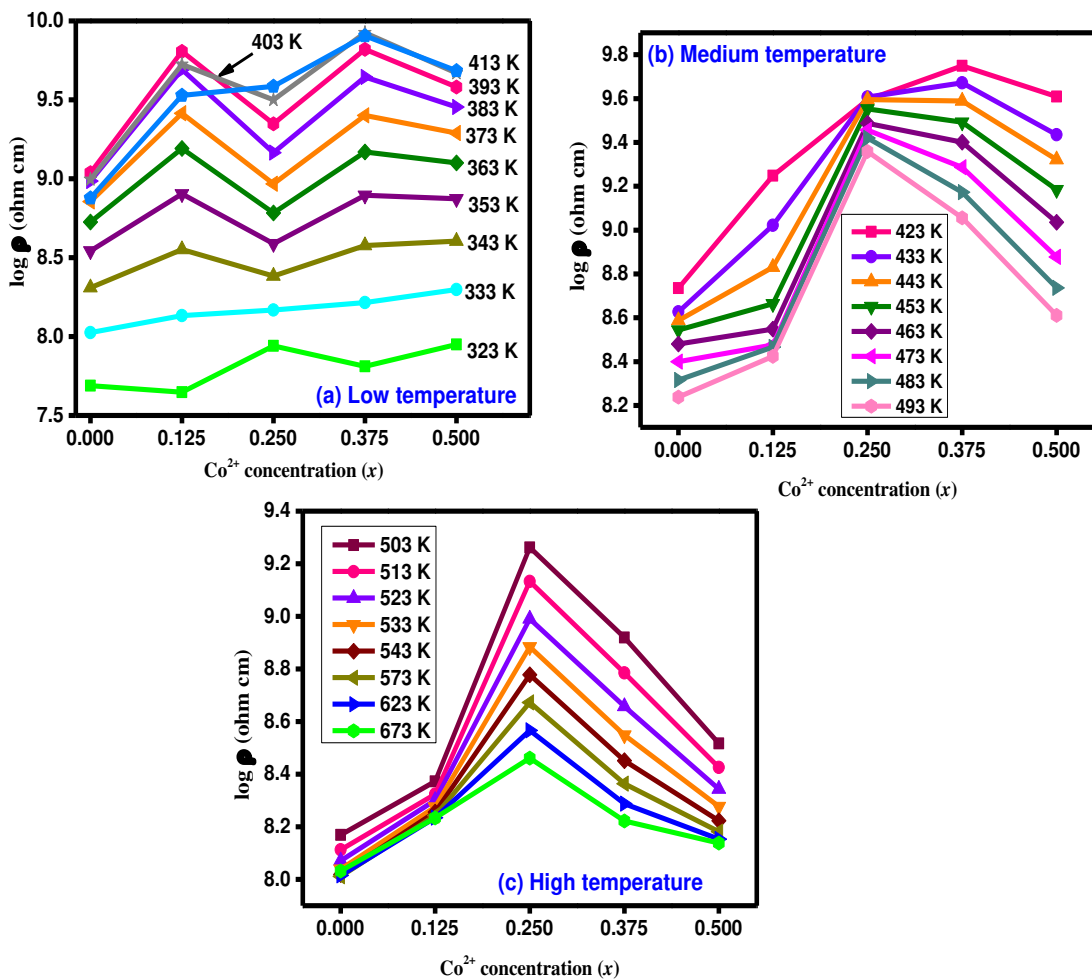
Fig. 12 Co^{2+} concentration (x) *versus* (**a**) log of resistivity (ρ) at low temperature (**b**) log of resistivity (ρ) at medium temperature (**c**) log of resistivity (ρ) at high temperature

23
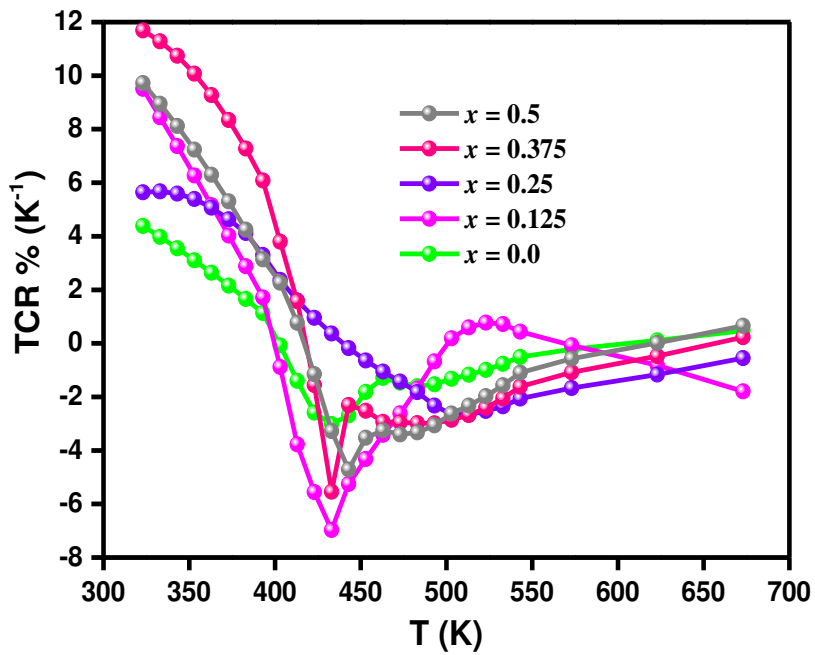
Fig. 13 Temperature *versus* TCR% for Co-MNCLF ferrites
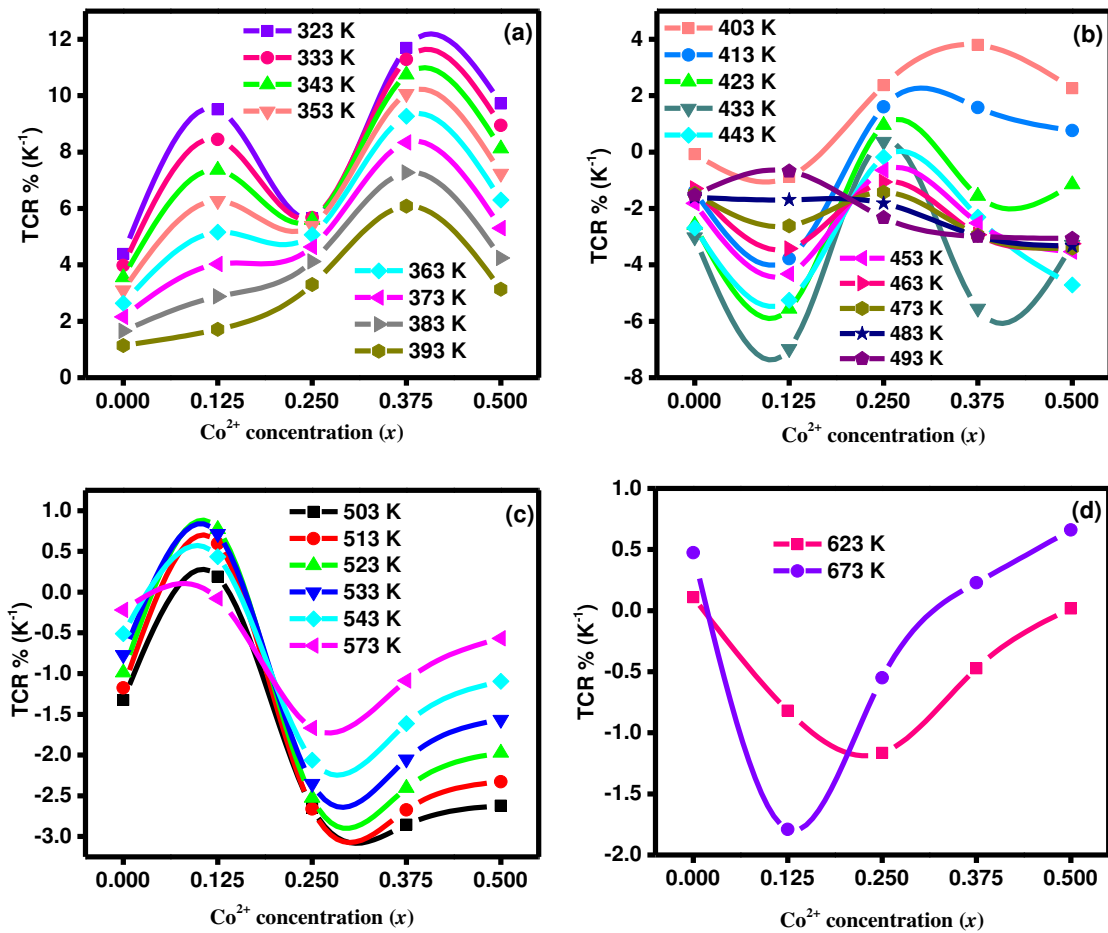
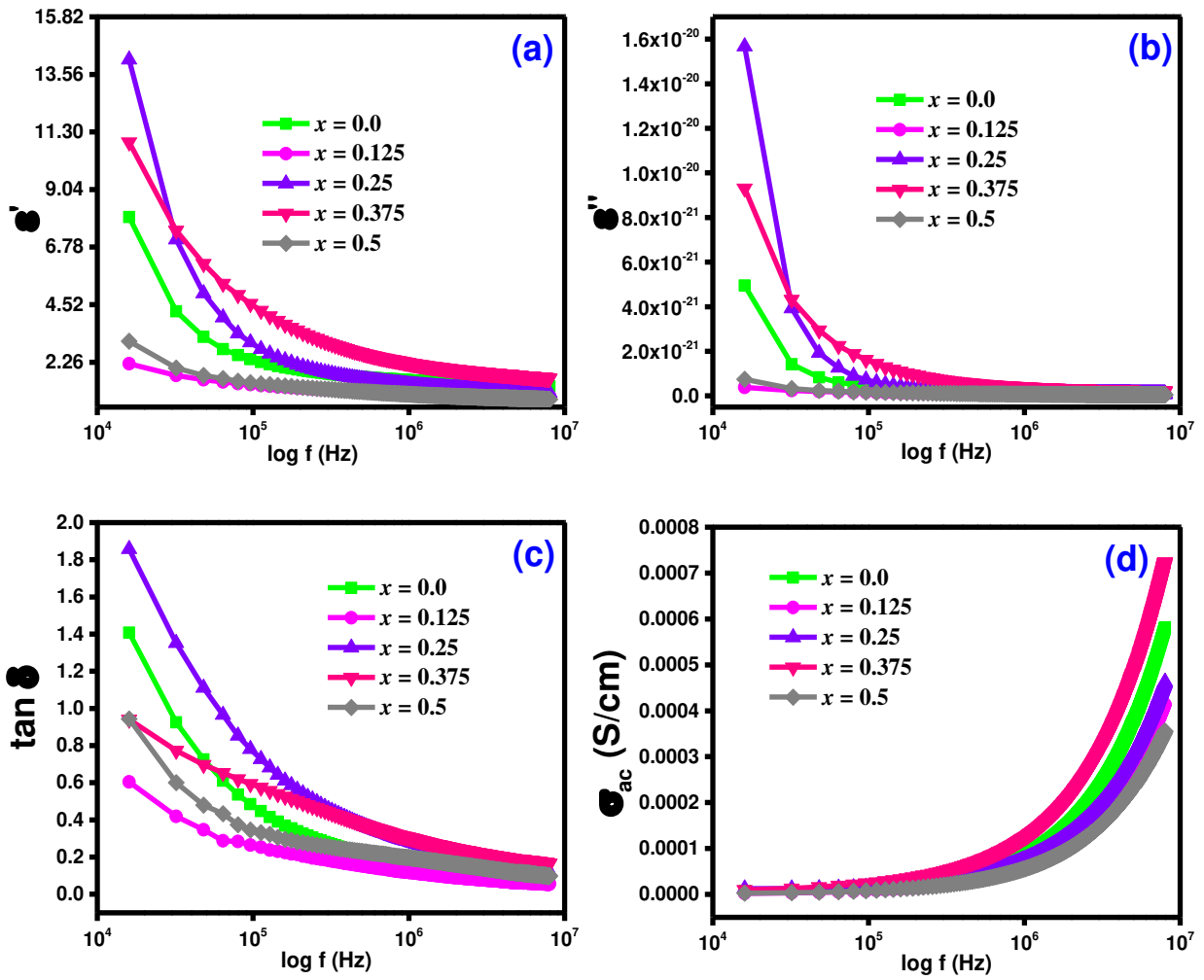**Fig. 14(a-d)** Co^{2+} concentration (*x*) *versus* TCR % at different temperatures

Fig. 15 Log of frequency *versus* (**a**) dielectric constant (ε') (**b**) dielectric constant loss (ε'') (**c**) dielectric tangent loss (tan δ) (**d**) *ac* conductivity (σ_{ac}) for Co-MNCLF ferrites
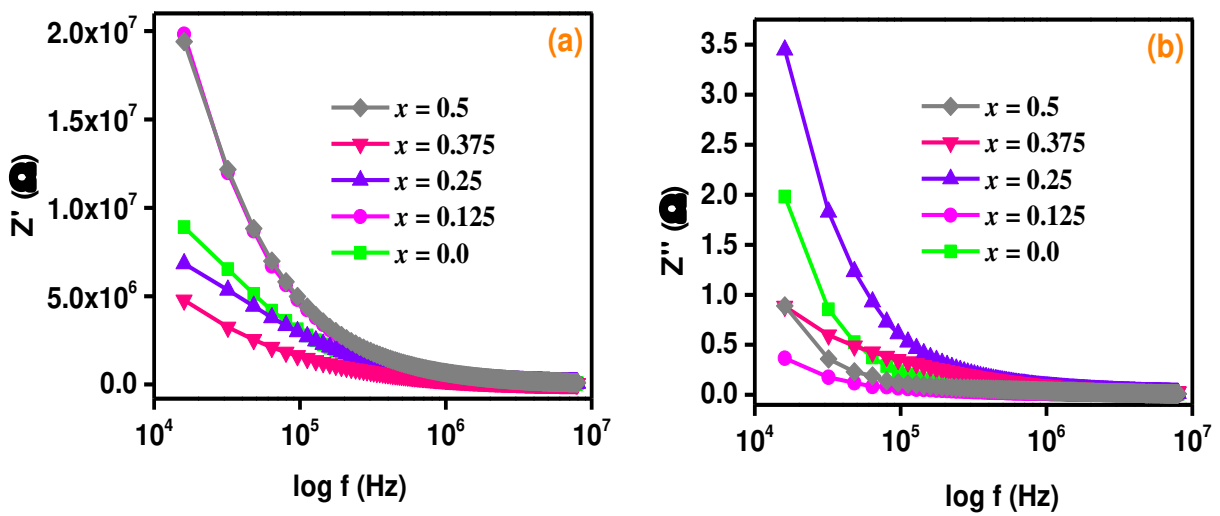
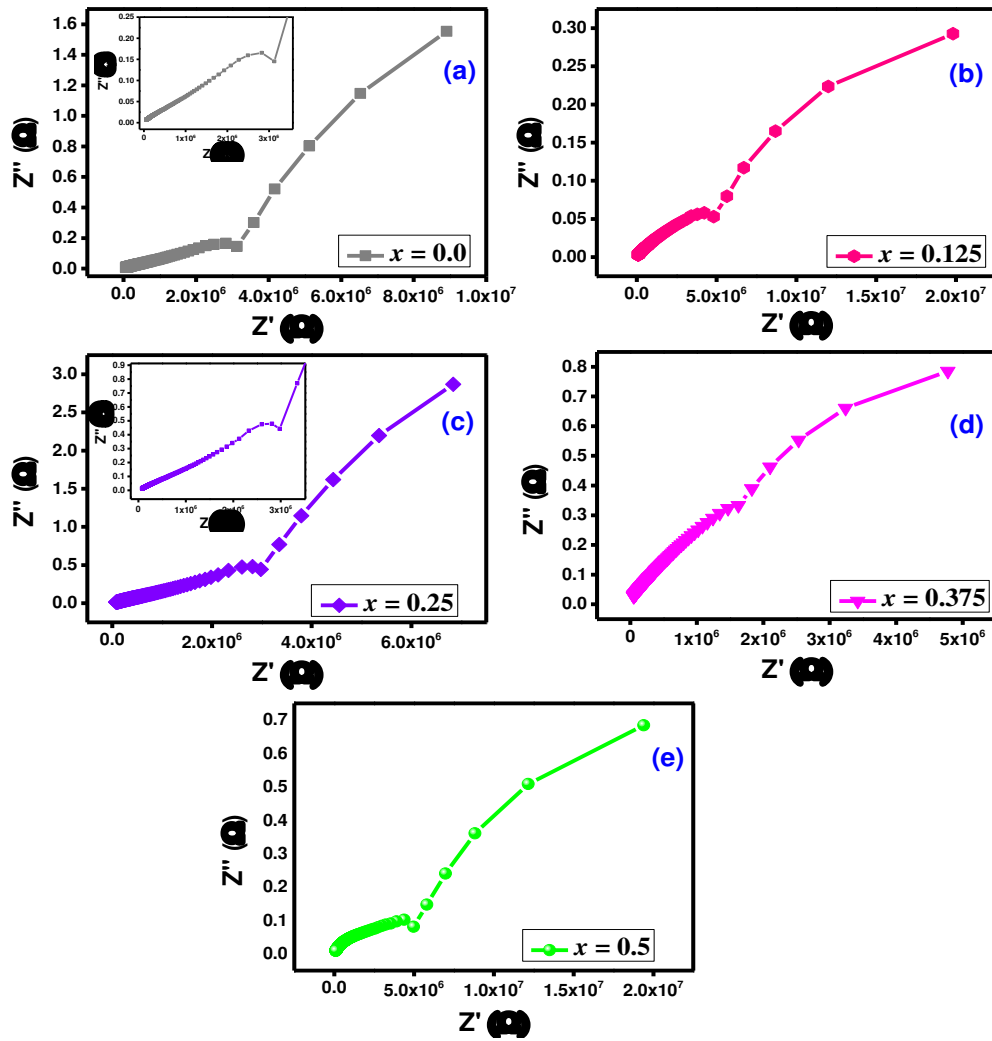**Fig. 16(a)** Log f *versus* real (**b**) imaginary part of impedance for Co-MNCLF ferrites

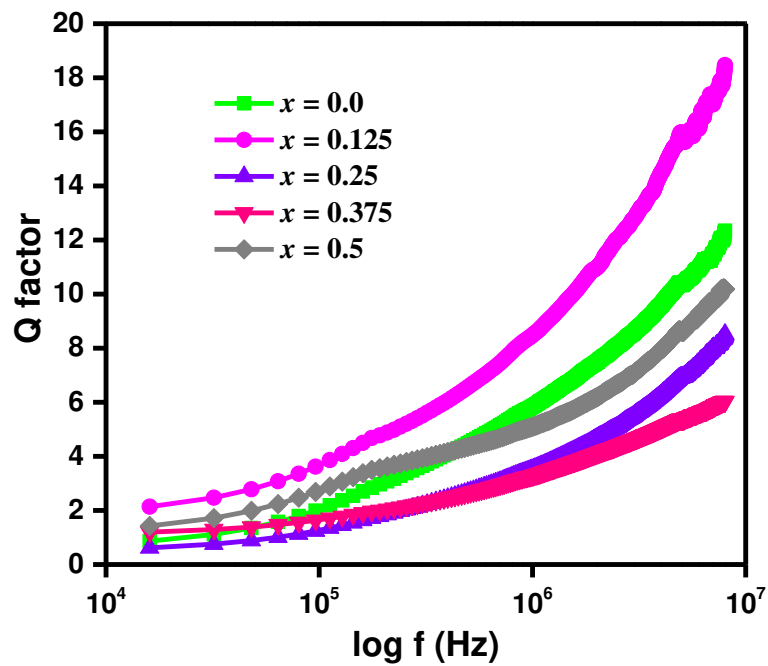**Fig. 17(a-e)** Cole-Cole (CC) plots for Co-MNCLF ferrites

Fig. 18 Plot of log f *versus* Q factor for Co-MNCLF ferrites

26